

Nowcast3D: Reliable precipitation nowcasting via gray-box learning

Huaguan Chen¹, Wei Han^{2,3*}, Haofei Sun⁴, Ning Lin¹, Xingtao Song⁵, Yunfan Yang^{6,7}, Jie Tian^{2,8}, Yang Liu⁹, Ji-Rong Wen^{1,10}, Xiaoye Zhang^{3,11}, Xueshun Shen^{2,3}, Hao Sun^{1,10*}

¹Gaoling School of Artificial Intelligence, Renmin University of China, Beijing, China

²Earth System Modeling and Prediction Center, China Meteorological Administration, Beijing, China

³State Key Laboratory of Severe Weather Meteorological Science and Technology, Beijing, China

⁴Shanghai Typhoon Institute, China Meteorological Administration, Shanghai, China

⁵School of Atmospheric Physics, Nanjing University of Information Science and Technology, Nanjing, China

⁶Institute of Atmospheric Physics, Chinese Academy of Sciences, Beijing, China

⁷College of Earth and Planetary Sciences, University of Chinese Academy of Sciences, Beijing, China

⁸Chinese Academy of Meteorological Sciences, China Meteorological Administration, Beijing, China

⁹School of Engineering Science, University of Chinese Academy of Sciences, Beijing, China

¹⁰Beijing Key Laboratory of Research on Large Models and Intelligent Governance, Beijing, China

¹¹Laboratory of Climate Change Mitigation and Carbon Neutrality, Henan University, Zhengzhou, China

*Corresponding authors

Abstract

Reliable nowcasting of extreme precipitation remains a major challenge, owing to the strongly nonlinear, multiscale, and nonstationary nature of convective systems in 3D space. Radar observations offer the backbone of nowcasting, yet existing methods struggle to faithfully predict extreme precipitation evolution: physics-based extrapolation falls short in capturing growth and decay, purely deterministic data-driven methods often produce over-smoothing prediction and underestimate extremes, and purely generative models usually lack physical consistency. While hybrid schemes that blend machine learning with physical principles are promising, they remain confined to 2D composite radar reflectivity. This collapses the atmosphere into a single layer and discards the critical vertical structure, thereby hindering accurate modeling of height-dependent dynamics. We introduce Nowcast3D, a gray-box, fully 3D nowcasting framework that operates directly on volumetric radar reflectivity. The end-to-end learning model integrates physically constrained neural operators (encoding advection, local diffusion, and microphysical processes) with a conditional diffusion model to generate ensemble forecasts with quantified uncertainty. Trained on provincial-scale 3D radar volumes spanning a $10.24^\circ \times 10.24^\circ$ region and fine-tuned on data in a $2.56^\circ \times 2.56^\circ$ city-scale region ($0.01^\circ \approx 1$ km), Nowcast3D delivers near-real-time radar-reflectivity forecasts with lead times up to 3 hours. It performs robustly and remains superior compared with several competitive baselines in both cross-region and temporal-out-of-sample evaluations. Notably, Nowcast3D is also capable of inferring wind fields without any labeled training data, supporting the physical plausibility of the learned transport dynamics. In a nationwide blind evaluation by 160 meteorologists, Nowcast3D ranked first for its competitive performance and was preferred in 57% of post-hoc assessments, surpassing the leading baseline (27%). These results highlight its potential of reliability and operational value for extreme precipitation nowcasting.

Keywords: Precipitation nowcasting, 3D volumetric radar reflectivity, Physics-guided learning

Introduction

On 16 June 2024, extreme rainfall struck multiple locations in Meizhou, Guangdong Province, China. The resulting floods and landslides in Pingyuan County, Jiaoling County and Meixian District caused several rivers to exceed historically recorded levels, impacted over 160,000 people across eight administrative regions, and resulted in 55 individuals dead or missing. Such events starkly illustrate the severe threat posed by intense precipitation to lives and infrastructure. They also highlight the pressing need for nowcasting systems capable of delivering longer lead times and higher accuracy, in order to facilitate timely warnings and improve risk mitigation.

Accurate short-term precipitation forecasting is critical for pre-disaster planning. However, the rapid evolution of intense rainfalls across a wide range of spatial and temporal scales poses severe challenges to both traditional numerical models and emerging data-driven methods [1]. Weather radar provides an observational foundation well-suited to this task. Modern radar networks acquire three-dimensional (3D) reflectivity fields with a horizontal resolution approaching 0.01° (≈ 1 km), minute-scale temporal sampling, and vertical spacing of a few hundred meters, yielding dense volumetric measurements of precipitating systems [2–4]. Radar reflectivity is closely related to instantaneous precipitation intensity. Consequently, time sequences of 3D radar data capture not only the movement of precipitation patterns but also the vertical structure of reflectivity. Variations in echo-top height, bright-band signatures, and layer-dependent reflectivity are closely linked to the initiation, growth, and propagation of convection, which strongly governs the evolution and organization of heavy precipitation [5, 6].

Numerical weather prediction (NWP) remains indispensable from synoptic to subseasonal scales, as it explicitly integrates the governing equations of motion and thermodynamics. However, operational NWP systems are constrained by update cycles, domain size, and computational cost, which limit the refresh rate and spatial resolution of forecasts. These limitations reduce their effectiveness for capturing rapidly evolving convection events [7]. While deep learning efforts to accelerate or emulate NWP have achieved gains in speed and scalability [8–14], these models are trained on global or regional NWP data. Consequently, they typically inherit a coarse grid spacing of tens to hundreds of kilometers and hourly output frequency, which falls short of the resolution required for convective nowcasting requirements.

Radar-observation-based forecasting methods remain the dominant paradigm for precipitation nowcasting. physics-based extrapolation techniques, such as pySTEPS [15], infer motion from recent fields and then advect them forward in time. Although these methods can preserve large-scale transport and achieve good skill at very short lead times, their positional and intensity errors grow rapidly as the lead time increases. End-to-end data-driven models trained on extensive radar archives have shown a great potential, e.g., DGMR [16], SimVP [17], among others [18–21]. However, in the absence of explicit physical constraints, their forecasts tend to over-smooth and weaken intense convective features, limiting their reliability for applications that depend on accurate prediction of extreme events.

Hybrid learning approaches that embed physical processes into neural networks have emerged to narrow this gap [22]. For instance, NowcastNet [1] unifies physical-evolution schemes and conditional-learning methods, thereby anchoring forecasts to transport dynamics and enhancing the physical coherence of prediction. However, notable limitations remain. Many existing hybrid methods operate on 2D radar composites, most commonly the vertical maximum reflectivity (e.g., MAX(Z)). This discards critical information on the vertical structure of atmosphere and therefore fails to capture features that are central to many convective and frontal systems [2, 3], such as height-dependent air shear and differential motion between layers or echo-top evolution.

To address these limitations, we develop Nowcast3D, an end-to-end gray-box nowcasting net-

work that unifies physics-inspired neural operators and a conditional diffusion model, operating directly on 3D volumetric radar reflectivity. By modeling convective systems in 3D space, Nowcast3D explicitly resolves height-dependent the atmospheric structure and its temporal evolution. Specifically, the model learns to decompose the observed reflectivity dynamics into three physically interpretable fields: a 3D flow field that governs advective transport, a spatially varying anisotropic diffusion field that captures local dispersive spreading, and a residual source term that accounts for unresolved microphysical and convective contributions. These components form a physics-grounded yet learnable deterministic core that advances forecasts under explicit constraints. To correct for prediction errors and represent uncertainty, this core is coupled with a diffusion model, conditioned jointly on both the input radar observations and the physics-informed forecast, to produce ensemble predictions for robust uncertainty quantification.

Nowcast3D was trained on provincial-scale 3D radar volumes covering a $10.24^\circ \times 10.24^\circ$ region at 0.04° resolution (approximately 3~4 km), and subsequently fine-tuned on data of a city-scale $2.56^\circ \times 2.56^\circ$ region at 0.01° resolution (approximately 1 km), enabling near-real-time forecasting with lead times up to 3 hours. In cross-region generalization tests and temporal-out-of-sample evaluations, Nowcast3D demonstrates robust performance and consistently outperforms several competitive baselines. Notably, the model can also infer physically plausible wind fields without any labeled wind supervision. The comparison with wind-profiler radar observations confirmed the physical consistency of the inferred latent transport dynamics. Finally, in a blind evaluation involving 160 meteorologists from 30 provinces (or municipalities) in China, the performance of Nowcast3D ranked first and was preferred in 57% of post-hoc assessments, highlighting its potential to improve the reliability and operational utility for extreme precipitation nowcasting.

Nowcast3D

Nowcast3D is designed to forecast precipitation, in particular extreme events, based on volumetric radar reflectivity. The core idea is to decompose complex atmospheric evolution into physically interpretable components and establish a unified learning architecture that couples a physics-inspired deterministic extrapolation network with a diffusion-based generative model for probabilistic forecasts (see Figure 1).

Our methodology decomposes the evolution of radar reflectivity into three dominant physical processes: advection, which captures the coherent drift of hydrometeors by 3D flow; local turbulent diffusion, representing the spreading of echoes toward neighbouring grid points due to small-scale mixing; and a microphysical tendency that accounts for in-situ mass and phase changes (Figure 1a) [23]. In this formulation, the advective field specifies, at each grid point, a dominant direction of motion, whereas the diffusive term relaxes the assumption of a single trajectory and allows reflectivity to fan out locally rather than move rigidly along a unique path. This advection–diffusion–microphysics decomposition provides a compact and interpretable description of reflectivity dynamics and serves as a strong prior for the deterministic core of Nowcast3D. The overall architecture consists of two tightly coupled stages (Figure 1b): a physics-driven prediction module and a probabilistic generation module. The physics-driven module first produces a single, dynamically constrained deterministic forecast, which then serves as a reference state. The generative module constructs an ensemble of plausible future evolutions based on the reference, thereby capturing the intrinsic uncertainty of precipitation development. An overview of the full Nowcast3D pipeline is depicted in Extended Data Figure 1, with detailed formulations presented in the [Methods](#) section.

The physics-driven module (Figure 1c) extrapolates the radar field using a neural network to infer the governing processes from a sequence of past observations and spatiotemporal embedding.

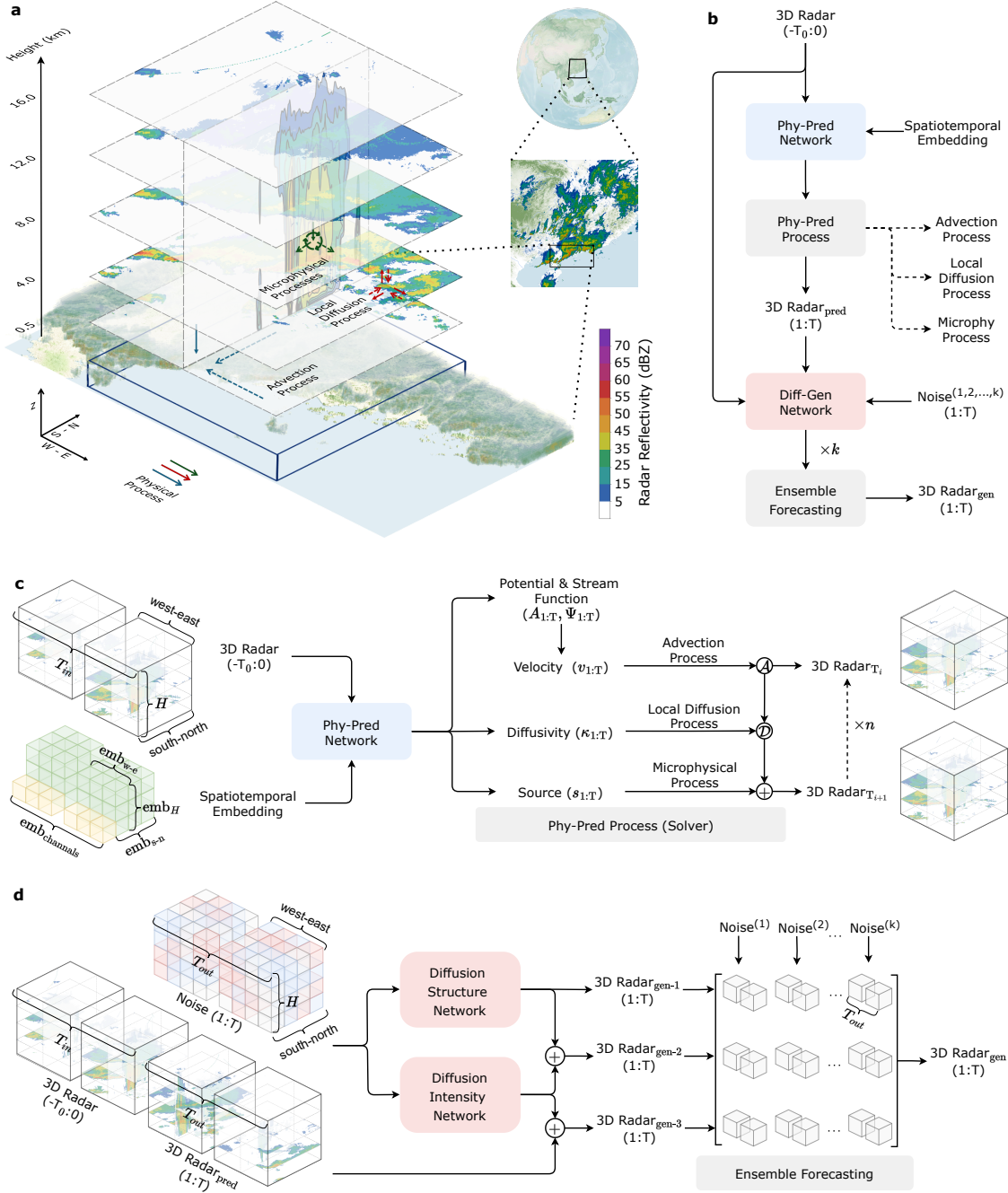


Figure 1: Schematic of the Nowcast3D model. **a**, Physical decomposition of reflectivity evolution. The changes in 3D radar reflectivity are decomposed into three contributions: advection by the 3D wind field, local diffusion capturing small-scale spreading, and microphysical tendencies that modify reflectivity in situ. **b**, Overall model architecture. The Phy-Pred Network infers latent physical fields from input 3D radar with spatiotemporal embedding, and a physics-based predictor advances the system according to the three processes in **a**. The resulting physics forecast conditions a diffusion generator which produces an ensemble of probabilistic forecasts via drawing multiple independent noise realizations. Details of Nowcast3D are provided in Extended Data Figure 1. **c**, Deterministic physics backbone (the Phy-Pred Process). The deterministic predictor performs each temporal update by explicitly applying advection, diffusion, and microphysical operators within the Phy-Pred Process module. **d**, Diffusion-based probabilistic generation (the Diff-Gen Network). The diffusion model learns physics-consistent mesoscale structure by the Diffusion Structure Network and stochastic residual components by the Diffusion Intensity Network. Under fixed conditioning, different sampled noise trajectories produce calibrated probabilistic 3D reflectivity forecasts.

In a single forward pass, an encoder processes the historical 3D radar volumes and outputs complete spatiotemporal fields of (i) an advective drift velocity, (ii) a local diffusion field, and (iii) a residual source term over the entire forecast horizon. Rather than explicitly reconstructing a sparse 3D velocity field, one branch of the network predicts scalar potential and vector stream-function fields, which are combined through a Helmholtz decomposition [24–26] to produce a more spatially continuous drift velocity field. In parallel, other network components infer a spatially varying, anisotropic diffusivity tensor that governs the local spreading of echoes, and a source field representing the net effect of microphysical processes. As summarized in Eq. (7), the final deterministic forecast is obtained by numerically solving the advection–diffusion–source system defined by these three operators, using the last observed radar state as the initial condition and the network-inferred fields as the governing parameters. The configuration of the spatiotemporal embeddings is given in [Supplementary Note 1.5](#). A detailed description of the model architecture and implementation is provided in [Supplementary Note 2.1](#). The analysis of the individual physical terms, together with comparisons to variants that learn the velocity field directly, is given in [Supplementary Note 5.1](#).

The probabilistic refinement stage is implemented via a conditional diffusion model with a dual-branch architecture (Figure 1d) [27–31]. Both diffusion branches are conditioned on the same context, consisting of the past 3D radar volumes and the physics-driven deterministic forecast, so that the generative model remains anchored to the physically constrained evolution. The first branch (aka, the structure network) learns to generate a full 3D reflectivity field that captures the overall spatial and temporal organization of echoes over the forecast horizon. The second branch (aka, the intensity network) learns a residual intensity field relative to the deterministic forecast, representing scale-localized amplification or weakening of precipitation intensity on top of the baseline solution. Using these two components, we can construct several types of samples: a purely generative structural realization, an intensity-refined deterministic forecast, and a sample that combines the generated structure with the learned intensity residual. As summarized in Eq. (8), drawing multiple independent noise vectors and propagating them through both diffusion branches under the shared conditioning yields a multi-member ensemble of 3D reflectivity forecasts. This provides a quantification of uncertainties in both spatial organization and intensity [32]. A detailed description of the model architecture and implementation is provided in [Supplementary Note 2.2](#). Examples of individual ensemble members, together with results from an ablation variant without the probabilistic refinement module, are shown in [Supplementary Note 5.2](#).

Evaluation settings

We evaluate the predictive skill and potential operational utility of Nowcast3D against three types of competitive baselines including extrapolation-based, purely data-driven, and hybrid nowcasting models (pySTEPS [15], SimVP [17], and NowcastNet [1], respectively). Specifically, the operational convective extrapolation approach pySTEPS [15] serves as a physics-informed reference widely used in national meteorological services. SimVP [17], a deep learning model originally developed for generic video prediction, is considered as a competitive purely data-driven baseline. NowcastNet [1] is included as a hybrid baseline, which integrates physics-informed priors with generative modeling and has demonstrated expert-validated operational value.

All models are trained and evaluated on large-scale radar observations in China. The primary training dataset consists of fixed-length radar sequences covering a $10.24^\circ \times 10.24^\circ$ region at 0.04° resolution in South China (Huanan area) during 2024, a region chosen for its diverse convective regimes. To assess cross-regional generalization, we evaluate the models on an independent test dataset in North China (Huabei area), having no geographical overlap with the training domain.

To further examine the performance in high-resolution urban settings, we design a dedicated experiment in a city-scale $2.56^\circ \times 2.56^\circ$ region (Maoming, Guangdong Province, China) at 0.01° resolution. In this experiment, Nowcast3D and all other learning-based methods are first pretrained on the South China dataset and then fine-tuned on a subset of 0.01° radar sequences collected in Maoming during 2024, while an independent 2025 Maoming subset held out for testing. Note that Nowcast3D is directly trained on native volumetric (3D) radar data, whereas all the baseline models are trained on 2D column-maximum reflectivity derived from the same volumes to ensure a fair comparison. Across all the experiments, models share identical input–output horizons and preprocessing pipelines. Hyperparameters for all learning-based models are tuned on a dedicated validation set, and the best-performing checkpoint is used for final testing. No other external data are used.

Our evaluation framework employs three complementary metrics to jointly assess the forecast quality. First, to quantify location-aware event detection, we use the neighborhood Critical Success Index (CSI) [33], which evaluates hits, misses and false alarms within prescribed radii at multiple reflectivity thresholds. Second, to evaluate the realism of predicted precipitation structures across spatial scales, we analyze the power spectral density (PSD) [34], comparing spectral slopes and power ratios of forecasts against observations from convective to mesoscale ranges. Third, to measure perceptual similarity and structural fidelity, we employ the Learned Perceptual Image Patch Similarity (LPIPS) metric [35]. For a fair comparison with the 2D baselines, all these three metrics are evaluated on column-maximum reflectivity fields, obtained by applying the same vertical projection to the three-dimensional Nowcast3D forecasts.

It is noted that, beyond standard reflectivity-based metrics, the unique capability of Nowcast3D to reconstruct the underlying atmospheric motion enables direct physical validation. We therefore verify its predicted 3D wind fields against co-located measurements by wind-profiler radars and ground-based weather stations at multiple altitudes.

Large-scale forecast at 0.04° resolution

We evaluate our model performance on the extreme precipitation event that affected Beijing, China on July 28, 2025. This event triggered a red heavy-rain warning (the highest level in China’s warning system) from the Beijing Meteorological Observatory, and resulted in substantial societal impacts, including 30 reported fatalities. Our analysis focuses on the period of most intense convection, from 15:00 to 18:00 UTC, during which the storm evolved rapidly and developed complex internal structures (Figure 2a).

The storm system comprised two main convective cells. A western cell moved eastward, producing broad, mainly moderate rainfalls. The eastern cell, situated closer to Beijing, remained the primary hazardous core with persistently high reflectivity. Over time, the two systems became more organized and gradually merged, with the heaviest rainfall region evolving into a pronounced V-shaped echo. One arm of this V extended eastward, while the other stretched southwest. Their motions differed: the eastern arm continued drifting eastward, whereas the southwestern arm shifted slightly southwest before becoming nearly stationary. This contrasting motion created strong differential movement within the system, continually reshaping the echo and posing two key challenges for forecasting: capturing the evolving morphology, and maintaining extreme rainfall intensity without artificial smoothing or rapid decay.

A comparison of the predicted and observed radar sequences highlights clear differences among different methods (Figure 2g). The SimVP forecast exhibits rapid loss of intensity and considerable distortion of the storm structure. pySTEPS and NowcastNet better preserve reflectivity amplitudes

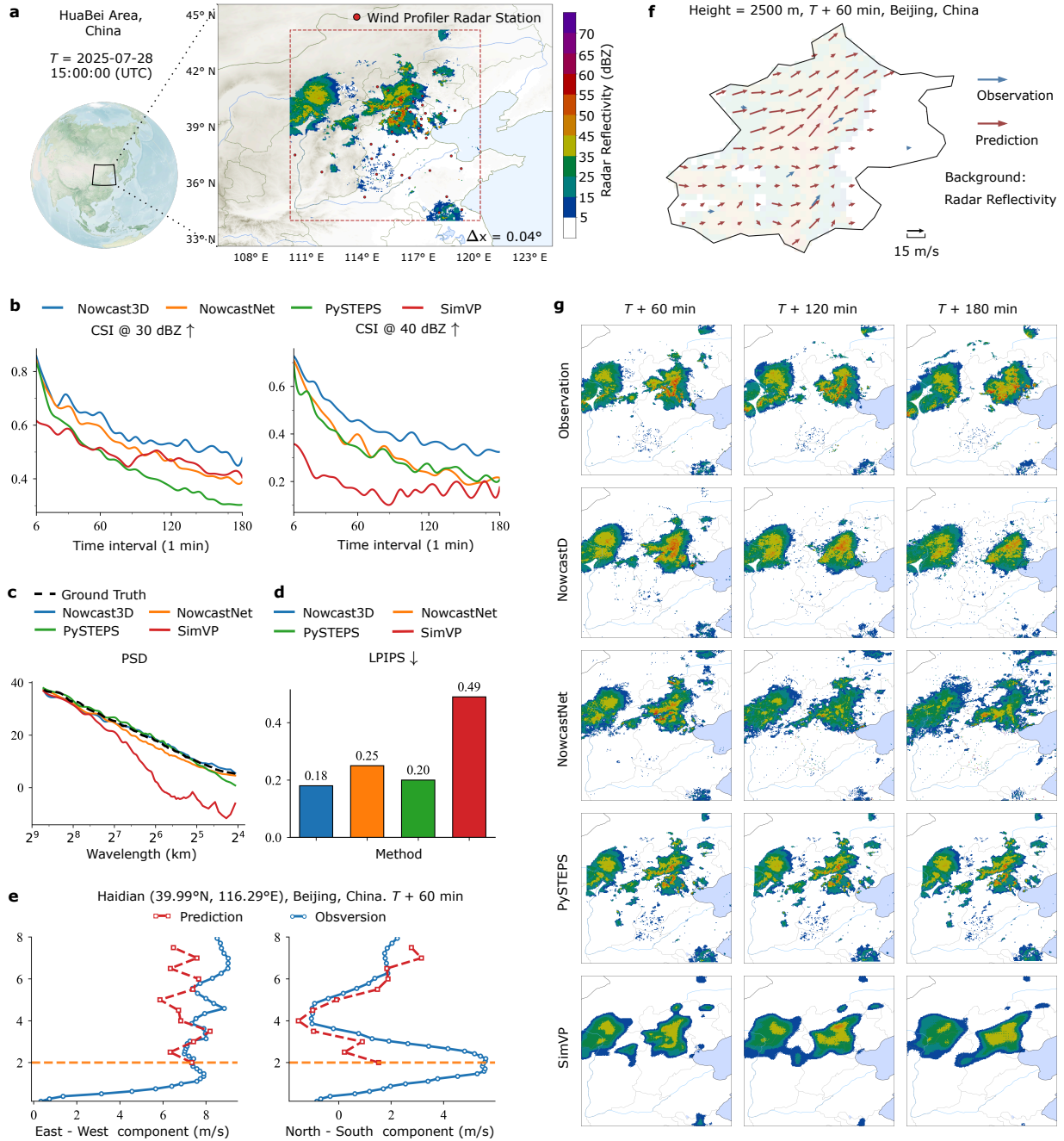


Figure 2: Nowcast3D accurately forecasts the evolution of a severe mesoscale convective system ($T = 15:00:00$ pm, July 28, 2025). **a**, Radar reflectivity of the convective system over North China at the forecast initialization time. The black box indicates the forecast domain, and red dots mark the locations of wind-profiler radar stations. **b**, Quantitative comparison of forecast skills in context of CSI at 30 dBZ and 40 dBZ reflectivity thresholds over a 3-hour forecast horizon. **c**, Analysis of spatial scale fidelity based on PSD. The forecast spectra are compared to the observed spectrum (black dashed line). **d**, Perceptual similarity assessment based on the LPIPS metric. Lower values indicate better performance. **e**, Vertical wind profile validation at a station located in Haidian district, Beijing. The predicted zonal (east–west) and meridional (north–south) wind components are compared with wind profiler observations at the 60-min lead time. **f**, Comparison of the predicted horizontal wind field with wind-profiler observations in Beijing at 2,500 m altitude (60-min lead time forecast). **g**, Forecast reflectivity fields by Nowcast3D and baseline models, compared with the observed radar sequence. The frame-by-frame comparison at 6-min intervals is provided in [Supplementary Video 1](#).

and sharp gradients, but exhibit large position errors and fail to reproduce the detailed evolution of the hazardous eastern cell. In contrast, Nowcast3D closely follows the complex evolution of the system, accurately tracking the displacement of the eastern cell while maintaining its internal structure and high reflectivity. These qualitative findings are supported by quantitative metrics. Nowcast3D achieves consistently higher neighborhood CSI scores across all lead times, indicating more accurate prediction of heavy-rainfall locations (Figure 2b). Nowcast3D also outperforms all the baselines in both PSD and LPIPS metrics, demonstrating more realistic small-scale variability and higher perceptual similarity to the observed radar fields (Figure 2c,d).

An important feature of our framework is its ability to infer the internal 3D wind field. To evaluate this physical component, we compare the predicted winds with independent observations from wind-profiler radars. Figure 2f shows the predicted horizontal wind field at 2,500 m altitude over Beijing a 60-min lead time, which aligns with co-located profiler measurements. Figure 2e further displays the vertical wind profiles at a station located in Haidian district, Beijing. The model reproduces the overall structure of both the zonal (east–west) and meridional (north–south) wind components capturing similar magnitudes throughout. While some deviation is seen in the zonal trend but similar magnitudes, the meridional component shows closer agreement. Layer-by-layer comparisons of the 3D radar reflectivity forecasts are provided in Extended Data Figure 2.

The inferred velocity field represents the motion of hydrometeors and is therefore most reliable in regions with substantial radar reflectivity. Its accuracy is inherently limited in echo-free areas and where low-level radar coverage is sparse. Within the precipitating volume, however, the model produces a dynamically consistent, high-resolution wind field that complements the spatially sparse measurements by ground-based stations. The calculation and evaluation of this wind field are summarized in Extended Data Figure 4, and the velocity field derived from the stream-function and potential-function decomposition is detailed in [Supplementary Note 6.2](#). Another precipitation case study at a different time, together with forecast comparisons, is presented in [Supplementary Note 6.3](#) (see [Supplementary Figure 9](#) and [Supplementary Video 2](#)).

Medium-scale forecast at 0.01° resolution

To assess our model’s ability to generalize to finer spatial scales (a key requirement for urban and operational forecasting), we evaluate its performance on forecasting an extreme precipitation event in Maoming, Guangdong Province, China on August 16, 2025. In this case, all models are operated at a 0.01° spatial resolution (Figure 3a). This higher resolution resolves faster and more intricate atmospheric processes, thereby posing a demanding test of forecast skill.

The storm evolution was dominated by two convective cells moving eastward along the coast. The western cell, initially more compact, broadened and intensified significantly as it progressed, while the eastern cell translated eastward and gradually moved out of the forecast domain. The key forecasting challenge was thus to reproduce the evolving storm morphology under rapid advection, in particular, the rapid area growth of the western cell and the simultaneous displacement of the eastern cell, which together drove large changes in the reflectivity field.

Comparing the predicted spatiotemporal evolution at this high resolution reveals the challenge of forecasting such rapidly evolving radar fields (Figure 3g). The deep-learning baselines, NowcastNet and SimVP, reproduce the overall eastward motion but fail to capture the expansion of the western cell, resulting in fragmented and underdeveloped echoes. The parameter-free pySTEPS model underestimates the translation speed of the system and does not reproduce its area growth. In contrast, Nowcast3D more faithfully captures both the rapid eastward displacement and the structural expansion of the convective system.

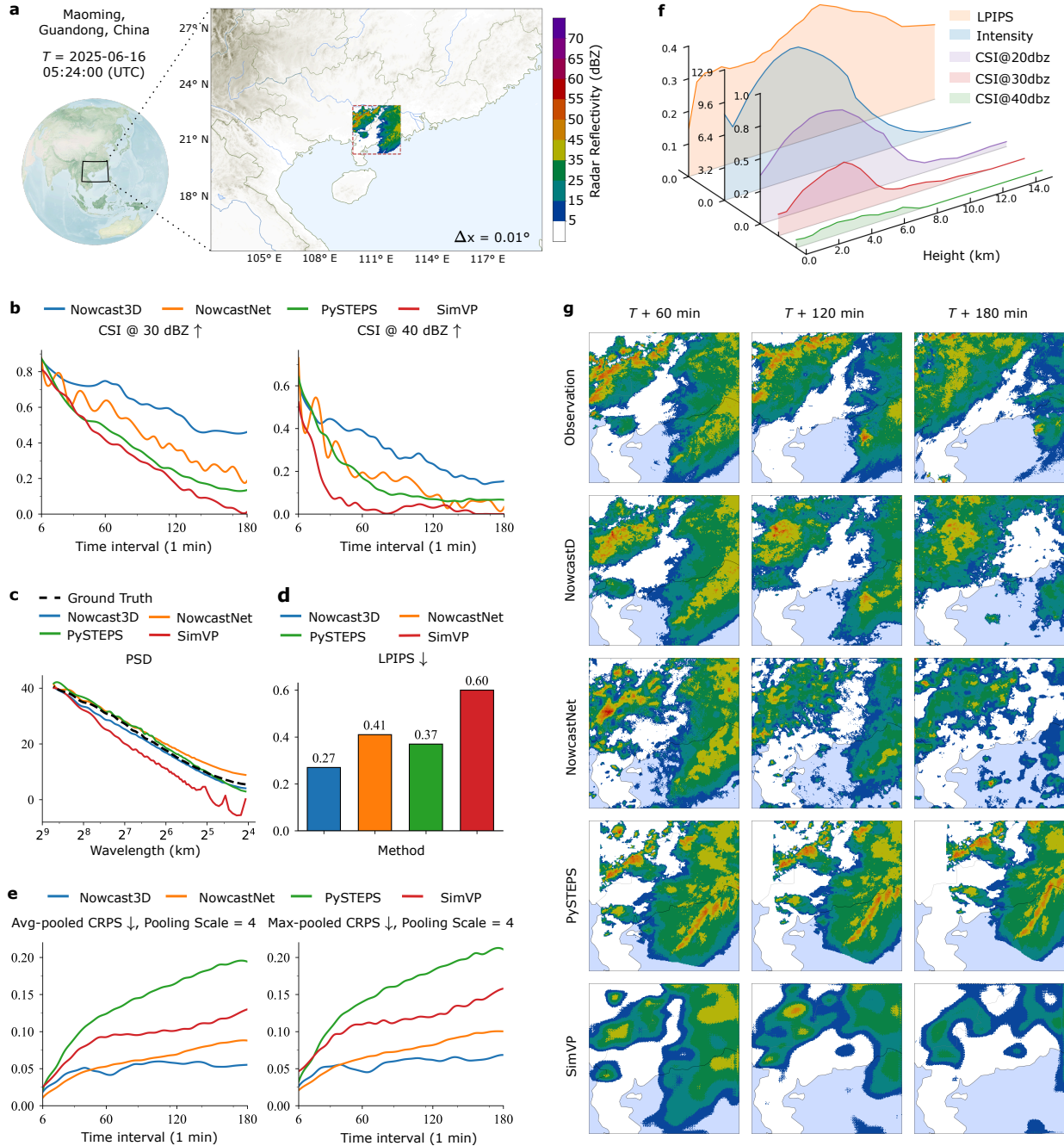


Figure 3: Generalization of Nowcast3D to high-resolution, fine-scale forecasting ($T = 13:54:00$ pm, June 17, 2025). **a**, Radar reflectivity over Maoming, Guangdong Province, China at the forecast initialization time. The analysis was conducted at 0.01° resolution. **b**, Quantitative comparison of forecast skills in context of CSI at 30 dBZ and 40 dBZ reflectivity thresholds over a 3-hour forecast horizon. **c**, Analysis of spatial scale fidelity based on PSD. The forecast spectra are compared to the observed spectrum (black dashed line). **d**, Perceptual similarity assessment based on the LPIPS metric. Lower values indicate better performance. **e**, Probabilistic forecast skill evaluated using the CRPS metric, shown as both average-pooled and max-pooled values. Lower scores indicate better-calibrated ensemble forecasts. **f**, Vertical profiles of forecast error and skill. CSI and LPIPS are plotted as a function of height, overlaid with profiles of mean observed reflectivity and data coverage. **g**, Forecast reflectivity fields by Nowcast3D and baseline models, compared with the observed radar sequence. The frame-by-frame comparison at 6-min intervals is provided in [Supplementary Video 3](#).

The quantitative results support these visual assessments. Nowcast3D substantially outperforms all baseline models in neighborhood CSI, indicating more accurate localization of precipitation (Figure 3b). In addition, PSD and LPIPS evaluations show that its forecasts better reproduce the observed scale-dependent variability and exhibit higher perceptual similarity to the radar observations (Figure 3c,d). Because Nowcast3D produces ensembles, we also assess its probabilistic forecast skill. The Continuous Ranked Probability Score (CRPS) [36, 37] shows that Nowcast3D yields better-calibrated forecasts than the ensemble-based NowcastNet, indicating more reliable uncertainty quantification (Figure 3e).

Taking advantage of our model’s native 3D design, we further examine the vertical distribution of forecast CSI (Figure 3f). A layer-wise analysis shows that CSI is lower near the surface and at upper levels, but higher in the mid-troposphere. This pattern closely mirrors the vertical profile of mean reflectivity: echoes are strongest and most organized at mid-levels, leading to higher CSI, whereas near-surface and upper levels exhibit weaker and more intermittent echoes, naturally yielding lower CSI. The resulting vertical CSI profile is therefore closely tied to both the intrinsic storm structure and the radar sampling characteristics, rather than representing a simple ranking of forecast skill with height. In contrast, LPIPS shows much smaller inter-layer variation, indicating that the model maintains a consistent perceptual quality of forecasts across different heights. Layer-by-layer comparisons of the 3D forecasts are provided in Extended Data Figure 3. Additional precipitation case studies together with forecast comparisons are presented in [Supplementary Note 6.3](#) (see [Supplementary Figures 10–11](#) and [Supplementary Videos 4–5](#)).

Meteorologist evaluation

To evaluate the practical utility of different models in forecasting extreme precipitation, we conducted an expert evaluation following the protocols established for DGMR [16] and NowcastNet [1]. A group of senior forecasters across China were invited nationwide. Forecast animations from all models were displayed side by side, anonymized and presented in random order to minimize bias.

A total of 160 meteorologists from the China Meteorological Administration and 30 provincial or municipal observatories participated in the evaluation. The demographic and regional distribution of participants is shown in Figure 4a. The experts cover nearly all regions of mainland China, except Tibet. Each meteorologist evaluated 23 test cases, randomly sampled from the precipitation events that occurred in China. Following the NowcastNet protocol [1], we considered two complementary evaluation modes. In the post-hoc mode, forecasters ranked the model forecasts with access to the verifying radar observations. In the prior mode, they conducted ranking only using the preceding radar sequences, without access to future observations, to simulate real-time operational decision-making in the real world.

The aggregated preferences are summarized in Figure 4b. In the post-hoc evaluation, Nowcast3D was ranked best in 57% of cases, while, in the prior evaluation, it remained the top choice in 51% of cases. Overall, Nowcast3D received the highest preference among the participating meteorologists. These preferences are consistent with the model’s ability to represent the 3D evolution of reflectivity, enabled by its explicit treatment of physical fields and embedded dynamical constraints. In contrast, the 2D baseline models showed limitations in reproducing the full spatiotemporal structure of precipitation systems. A detailed description of the expert evaluation configuration is provided in [Supplementary Note 4](#).

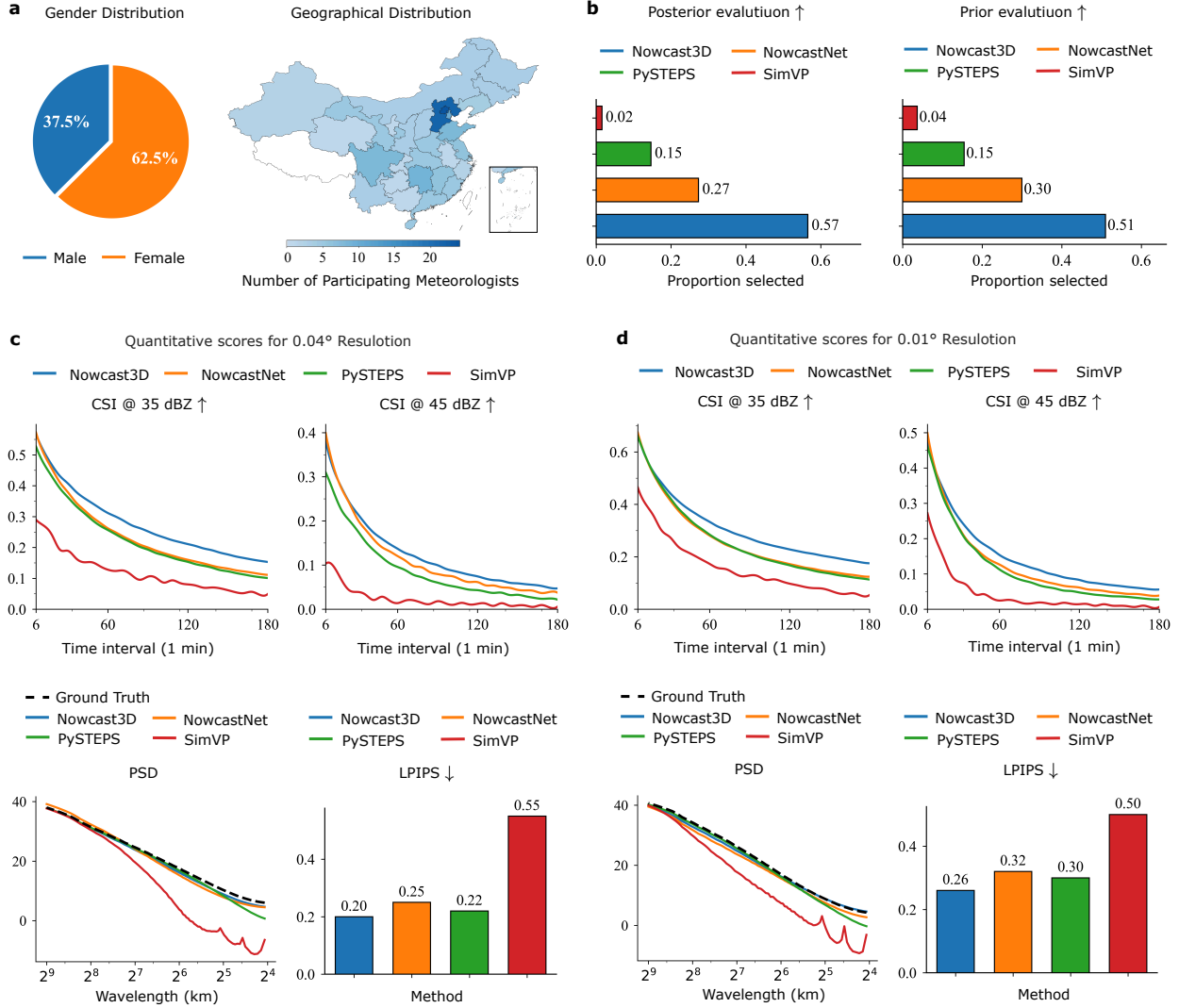


Figure 4: Aggregate quantitative evaluation of forecast skill. **a**, Demographics and institutional affiliations of the participating meteorologists, including gender and regional distribution. **b**, Evaluation of meteorologists’ model preferences. Compared with other competing baseline methods, meteorologists showed a stronger preference for Nowcast3D. **c**, Forecast skill metrics evaluated on the 0.04° resolution test set. The top panels show CSI as a function of lead time at 35 dBZ and 45 dBZ thresholds. The bottom-left panel shows PSD of forecasts compared with the ground truth (black dashed line), and the bottom-right panel shows the mean LPIPS scores, where lower values indicate better perceptual quality. **d**, The same set of metrics as in **c**, evaluated on the 0.01° resolution test set to assess the generalizability of different models at a finer spatial scale.

Quantitative evaluation

To quantify the forecast skill, we employ three complementary metrics: neighbourhood CSI to assess location-dependent event detection, PSD to evaluate scale-dependent spatial structure, and LPIPS to measure perceptual and structural similarity. All metrics are computed over the full test corpus at two spatial scales: a provincial-scale domain at a standard 0.04° resolution and a more demanding urban domain at 0.01° resolution. This dual-scale design allows us to examine the model’s performance and robustness to finer spatial details.

At 0.04° resolution, Nowcast3D consistently outperforms all baseline models across all metrics

(Figure 4c). For both moderate (35 dBZ) and intense (45 dBZ) reflectivity thresholds, it achieves the highest neighbourhood CSI throughout the 3-hour forecast horizon, indicating more accurate localization of heavy precipitation. The PSD analysis confirms that its forecasts most closely match the observed power spectrum, reflecting a more realistic representation of precipitation structures across spatial scales. This is corroborated by the LPIPS scores, where Nowcast3D attains the lowest values, indicating the highest perceptual and structural fidelity.

This advantage persists at the finer 0.01° resolution, which provides a stricter test of performance at the city scale (Figure 4d). Across all lead times and metrics, Nowcast3D maintains a clear margin over the competing baseline models, demonstrating that its architecture can be effectively adapted to finer spatial grids. Taken together, these results show that explicit modeling of 3D dynamics yields forecasts that are more accurate, structurally realistic and perceptually coherent than those produced by existing approaches. This benefit holds robustly across two different spatial scales.

Additional CSI curves over a wider range of intensity thresholds are provided in [Supplementary Note 6.1](#) (see [Supplementary Figure 5](#)).

Discussion

Precipitation nowcasting remains a central challenge in atmospheric science due to the strongly nonlinear, multiscale, and inherently non-stationary nature of convective evolution, which contains a substantial stochastic component. Although recent data-driven advances have improved short-range guidance, skill for extreme precipitation still degrades rapidly along with lead time. Existing approaches primarily operate on 2D radar products that collapse the atmosphere into a single layer, discarding the height-dependent organization of convection and the layer-to-layer wind variations that shape storm motion and intensity through vertical motion and shear. Consequently, purely 2D methods often lack the physical fidelity needed for reliable, operationally useful nowcasts in hazardous weather regimes.

Our work addresses these limitations by combining physics-informed dynamics with deep generative modeling on native 3D radar volumes. The core idea is establish a physics-informed operator network that learns to infer and extrapolate key physical drivers directly from sequences of volumetric reflectivity: a 3D wind field that governs advective transport, a local field that represents stochastic dispersion, and a residual tendency associated with unresolved microphysics. The forecast is advanced according to the learned operators, enforcing physical consistency and enabling physically plausible predictions at lead times. This physics-informed learning core is coupled to a conditional generative model that approximates the full distribution of future states, capturing uncertainty in both storm structure and localized intensity. Together, these components produce forecasts that are dynamically consistent and probabilistically reliable, delivering the uncertainty information required for risk-aware decision-making.

The performance of this framework nonetheless depends on several external factors. First, its accuracy is constrained by the quality, coverage and scanning strategy of the input radar network. The beam attenuation, ground clutter and anomalous propagation also remain important sources of error. Second, inferring 3D flow from reflectivity alone is under-constrained, particularly in regimes with complex microphysics where phase changes can alter reflectivity without a corresponding change in the velocity field. These limitations point to clear directions for future work. Integrating additional observation types, such as Doppler radial velocities, geostationary satellite imagery and lightning measurements, could better constrain the inferred wind fields and improve the realism of hydrometeor evolution. Closer coupling with numerical weather prediction models, for example through data assimilation of the learned fields or by using NWP output as a physical

prior, could further extend forecast skill beyond the traditional nowcasting range.

In conclusion, by unifying physics-informed dynamics with deep generative modeling on 3D radar data, this study outlines a pathway toward developing new nowcasting systems. Such models go beyond simple pattern extrapolation to learn representations of the underlying physical processes, producing forecasts that are more accurate, reliable and physically consistent. Further enriching this framework with multimodal observations and tighter NWP coupling has potential to close the remaining gap towards robust, actionable forecasts of extreme precipitation events — a capability urgently needed in practice.

Methods

Overview of the Nowcast3D framework

Nowcast3D is a hybrid forecasting system that combines a physics-informed neural predictor with a diffusion-based generative model to produce probabilistic 3D radar reflectivity forecasts. As summarized in Extended Data Figure 1, the workflow has three stages. First, raw volumetric radar observations are passed through a data-processing module that derives a 3D spatial mask of observed and unobserved regions, applies mask-guided imputation only in the unobserved regions, and normalizes reflectivity to a fixed dynamic range. Second, a physics-informed network infers underlying physical fields from the recent radar history and advances them forward in time based on an explicit advection–diffusion–source equation, thereby producing a deterministic forecast. Third, a conditional diffusion model refines this physics-consistent forecast into an ensemble of stochastic realizations that quantify forecast uncertainty.

In this framework, the preprocessing stage defines the input reflectivity fields R used throughout the paper. The physics-informed module implements a mapping, denoted by Θ , from the observed radar history to time-varying physical fields $X_{1:T}$ and a neural-numerical solver for the resulting evolution operator \mathcal{F} . The generative module implements a conditional diffusion model, denoted by Φ , that samples future trajectories conditioned on both past observations and the deterministic forecast. The following subsections describe the radar data and its preprocessing, the hybrid physics–generative formulation, the physics-informed forecasting module, the probabilistic refinement module, and the training procedure.

Radar datasets and preprocessing

Our forecasts are driven solely by 3D radar reflectivity from the national radar composite operated by the China Meteorological Administration. This product provides volumetric reflectivity on 24 constant-altitude levels between 0.5 and 16 km, with native horizontal resolutions down to 0.01°. These volumes resolve the 3D structure and evolution of precipitating systems over China and form the common input to all models evaluated in this study. Details of the dataset, including the storage format, are provided in [Supplementary Note 1.1](#).

We consider three study domains that together span diverse convective regimes and spatial resolutions. The primary training domain is located in South China (110.00°–120.24°E, 23.96°–34.20°N), where we use all eligible radar volumes recorded in 2024. Cross-regional generalization at the native 0.04° resolution is assessed on a subset of precipitating scenes over North China (110.00°–120.24°E, 33.96°–44.20°N) observed in 2025. This subset is spatially and temporally disjoint from the training domain of South China. High-resolution coastal precipitation hazards are evaluated over the Maoming region in Guangdong Province, China (109.64°–112.20°E, 20.39°–22.95°N), where pre-trained models at 0.04° resolution are fine-tuned on 0.01° Maoming sequences recorded in 2024.

An independent subset of Maoming precipitation events in 2025 is reserved for testing. The radar composite coverage and the three study domains are shown in Extended Data Figure 5a. Note that Extended Data Figure 5b illustrates how terrain blocking and the shorter range of low-elevation scans lead to a pattern of sparse, near-surface circular observations.

Before inputting into the forecasting model, raw radar volumes pass through a preprocessing pipeline (see Extended Data Figure 1b). We first construct a mask that flags regions with missing measurements, including areas affected by terrain-induced beam blockage and range limitations. A non-learning, mask-guided imputation scheme is then applied to fill only the masked regions, using upper-level reflectivity as a predictor while leaving all observed echoes unchanged. Finally, reflectivity values are normalized to a fixed dynamic range. Extended Data Figure 5c,d compare raw and imputation reflectivity fields at 500 m and 1,000 m over the South China and Maoming regions, respectively. Further details on masking, imputation, and normalization are given in [Supplementary Notes 1.2–1.4](#).

Hybrid physics–generative formulation

Let $\{R_t\}_{t=-T_0}^T$ denote the preprocessed 3D radar reflectivity sequence, where each $R_t \in \mathbb{R}^{D \times H \times W}$. $D \times H \times W$ are the vertical and horizontal grid dimensions. The past observations are written as $R_{-T_0:0} \in \mathbb{R}^{(T_0+1) \times D \times H \times W}$. Given $R_{-T_0:0}$, our goal is to forecast the future sequence $R_{1:T} \in \mathbb{R}^{T \times D \times H \times W}$ using a unified two-stage framework that first produces a physics-based deterministic forecast and then refines it by a probabilistic ensemble model.

In the physics-informed learning stage, a neural network Θ maps the historical radar sequence to a set of time-varying physical fields, $X_{1:T} = \Theta(R_{-T_0:0})$, where $X_{1:T} \in \mathbb{R}^{T \times C \times D \times H \times W}$ and C is the number of inferred quantities that govern the evolution of reflectivity. These fields act as coefficients in a time-dependent evolution equation, $\partial_t R = \mathcal{F}(R, X)$, where \mathcal{F} represents the physical dynamics controlled by X . Starting from the initial condition $R(0) = R_0$ (the last observed volume), integrating this equation forward in time yields a deterministic forecast $R_{1:T}^{\text{det}}$.

In the probabilistic forecasting stage, a conditional diffusion model generates an ensemble of forecasts around the physics-consistent trajectory produced by the deterministic core. The generative network Φ is conditioned on the context $c = \{R_{-T_0:0}, R_{1:T}^{\text{det}}\}$, which combines the past observations with the deterministic prediction. Ensemble members are obtained by sampling the learned conditional distribution with different noise realisations $\epsilon^{(k)}$, $k = 1, \dots, K$, thereby representing stochastic variability and forecast uncertainty.

The aforementioned steps can be written compactly as follows:

$$X_{1:T} = \Theta(R_{-T_0:0}), \quad X_{1:T} \in \mathbb{R}^{T \times C \times D \times H \times W}, \quad (\text{physical fields}) \quad (1.1)$$

$$R_{1:T}^{\text{det}} = \text{Solve}\left(\frac{\partial R}{\partial t} = \mathcal{F}(R, X), R(0) = R_0\right), \quad (\text{deterministic forecast}) \quad (1.2)$$

$$c = \{R_{-T_0:0}, R_{1:T}^{\text{det}}\}, \quad (\text{conditioning context}) \quad (1.3)$$

$$R_{1:T}^{(k)} = \text{Sample}_{\Phi}(\epsilon^{(k)}, c), \quad k = 1, \dots, K, \quad (\text{sampling}) \quad (1.4)$$

$$R_{1:T}^{\text{ens}} = \{R_{1:T}^{(k)}\}_{k=1}^K. \quad (\text{ensemble forecast}) \quad (1.5)$$

Nowcast3D implements these formulations with a shared backbone that realizes Θ and a conditional diffusion network that realizes Φ , as described in the following.

Physics-informed forecasting module

Network architecture. The physics-informed forecasting module (aka, the Phy-Pred Network shown in Extended Data Figure 1b) implements the mapping Θ in Eq. (1.1). An encoder first extracts multi-scale features from the preprocessed radar history $R_{-T_0:0}$. These features are processed by two complementary branches: a U-Net branch [38] that captures local and fine-scale structures, and a Transformer branch [39] that represents long-range spatial and temporal dependencies. Their outputs are fused into a common representation, which is then decoded into time-varying physical fields corresponding to advective motion, anisotropic diffusion and intensity tendency. These fields parameterize the evolution operator \mathcal{F} , and a numerical solver advances the last observed radar volume in time to obtain the deterministic forecast $R_{1:T}^{\text{det}}$.

Physical dynamics. We model the evolution of radar reflectivity in continuous time and space over a fixed forecast horizon. The deterministic forecast $R_{1:T}^{\text{det}}$ is obtained by numerically integrating a partial differential equation. We specify the dynamics $\mathcal{F}(R, X)$ as an advection–diffusion–source equation, given by

$$\frac{\partial R}{\partial t} = \underbrace{-\mathbf{v} \cdot \nabla R}_{\text{advection}} + \underbrace{\nabla \cdot (\boldsymbol{\kappa} \nabla R)}_{\text{diffusion}} + \underbrace{s}_{\text{source}}. \quad (2)$$

Here, the reflectivity field R evolves under three processes: advective transport by a 3D velocity field \mathbf{v} ; local anisotropic diffusion governed by a diffusivity tensor $\boldsymbol{\kappa}$; and a residual source term s that summarizes unresolved processes, including microphysical growth and decay. The time-varying fields $(\mathbf{v}, \boldsymbol{\kappa}, s)$ over the forecast horizon constitute the physical fields $X_{1:T}$ and are inferred from the input radar sequence $R_{-T_0:0}$ by the physics module Θ .

Neural parameterization. The time-varying physical fields $X_{1:T} = (\mathbf{v}_{1:T}, \boldsymbol{\kappa}_{1:T}, s_{1:T})$ required in Eq. (2) are produced by a shared encoder–decoder backbone followed by task-specific heads. We denote the backbone (encoder, U-Net branch, Transformer branch and fusion) by $\text{Backbone}(\cdot)$. Its output is passed to three dedicated decoders that specialize in motion, diffusion and source components, expressed as follows:

$$(\varphi_{1:T}, \boldsymbol{\psi}_{1:T}) = \text{Decoder}_{\text{Motion}}(\text{Backbone}(R_{-T_0:0})), \quad (3.1)$$

$$\boldsymbol{\kappa}_{1:T} = \text{Decoder}_{\text{AnisoBrown}}(\text{Backbone}(R_{-T_0:0})), \quad (3.2)$$

$$s_{1:T} = \text{Decoder}_{\text{Intensity}}(\text{Backbone}(R_{-T_0:0})), \quad (3.3)$$

where the full velocity field is reconstructed from a scalar potential φ and a vector potential $\boldsymbol{\psi}$ via $\mathbf{v}_{1:T} = \nabla \varphi_{1:T} + \nabla \times \boldsymbol{\psi}_{1:T}$. The backbone parameters are shared across all outputs, whereas the three decoders have separate parameters and specialize in inferring the dynamics of motion, diffusion and source terms, respectively. Additional architecture details are given in [Supplementary Figure 2](#).

Numerical extrapolation. Given the inferred fields $(\mathbf{v}_{1:T}, \boldsymbol{\kappa}_{1:T}, s_{1:T})$, we advance the radar field R_t forward in time by numerically integrating Eq. (2). We use an operator-splitting scheme that decomposes each time step into successive advection, diffusion and source updates. The advection operator that reads

$$\mathcal{A}_{\Delta t}[R_t](x) = R_t(x - \mathbf{v}_t(x) \Delta t) \quad (4)$$

is implemented using a semi-Lagrangian method [1, 40], which remains stable for large Courant numbers and is well suited to long lead times. To implement anisotropic diffusion, we exploit the

link between diffusion and random motion [41–43] and define the diffusion operator as

$$\mathcal{D}_{\Delta t}[R_t](x) = \mathbb{E}_{\eta \sim \mathcal{N}(0, 2\kappa_t \Delta t)} [R_t(x + \eta)], \quad (5)$$

where the expectation is taken over Gaussian displacements with covariance determined by κ_t . The source term is applied as an additive correction.

Composing these operators yields the one-step update expressed as

$$R_{t+1} \approx \mathcal{D}_{\Delta t}[\mathcal{A}_{\Delta t}[R_t]] + s_t \Delta t. \quad (6)$$

In practice, the expectation in the diffusion step is approximated by a Monte Carlo average over M samples. For a voxel at location x , the numerical update becomes

$$R_{t+1}(x) \approx \frac{1}{M} \sum_{m=1}^M R_t(x - \mathbf{v}_t(x) \Delta t + \eta_t^{(m)}(x)) + s_t(x) \Delta t, \quad (7)$$

where each stochastic displacement $\eta_t^{(m)}(x)$ is drawn independently from $\mathcal{N}(0, 2\kappa_t(x)\Delta t)$. Throughout both training and inference, we fix empirically the number of diffusion samples to $M = 8$.

Probabilistic refinement module

Network architecture. The diffusion-based generative network (aka, the Diff-Gen Network depicted in Extended Data Figure 1b) implements the mapping Φ in Eq. (1.4). We adopt a conditional generative architecture that explicitly incorporates historical information [30]: given the conditioning information $c = \{R_{-T_0:0}, R_{1:T}^{\text{det}}\}$, a ContextNet first encodes this information into a compact representation that summarizes both the recent observations and the trajectory of physics-informed forecasts. Conditional diffusion modules then take this context together with independent noise realisations and iteratively refine them into stochastic forecast trajectories. One branch focuses on the large-scale reflectivity pattern, while a residual diffusion branch learns local intensity corrections relative to the deterministic forecast. Different noise inputs produce a set of samples $\{R_{1:T}^{(k)}\}_{k=1}^K$, which together form the ensemble forecast $R_{1:T}^{\text{ens}}$ used for probabilistic evaluation and downstream decision-making (see Supplementary Figure 3 for architecture details).

Because the physics-informed learning module already advances the full 3D reflectivity field through explicit dynamical operators, the role of Φ is to provide a stochastic refinement around this baseline state. To reduce training complexity and computational cost, we implement this refinement in the 2D space, operating on full time sequences of radar cross-sections rather than on complete 3D volumes. The same trained network can subsequently be applied either to column-maximum reflectivity sequences to generate 2D probabilistic forecasts, or independently to sequences from multiple height levels, whose outputs can be stacked to reconstruct a 3D ensemble of reflectivity volumes. Further construction and sampling details are provided in Supplementary Note 2.2.

Ensemble construction. Operationally, the probabilistic refinement module implements the sampling step $R_{1:T}^{(k)} = \text{Sample}_{\Phi}(\epsilon^{(k)}, c)$ used to construct the ensemble forecast. For each noise realisation $\epsilon^{(k)}$, the two diffusion branches produce a pair of correlated outputs: a full-field structure $S_{\text{struct}}^{(k)}$ and a residual field $S_{\text{res}}^{(k)}$ defined relative to the deterministic forecast. This pair of

outputs supports three types of ensemble members constructed from each sample, namely,

$$S^{(1)} = S_{\text{struct}}, \quad (\text{full-field forecast}) \quad (8.1)$$

$$S^{(2)} = R_{1:T}^{\text{det}} + S_{\text{res}}, \quad (\text{physics-corrected forecast}) \quad (8.2)$$

$$S^{(3)} = S_{\text{struct}} + \alpha S_{\text{res}}, \quad (\text{hybrid forecast}) \quad (8.3)$$

where $\alpha \in [0, 1]$ is a mixing coefficient. Generating K independent noise realisations yields K pairs $\{(S_{\text{struct}}^{(k)}, S_{\text{res}}^{(k)})\}_{k=1}^K$, from which we form the ensemble:

$$R_{1:T}^{\text{ens}} = \{S_{1:T}^{(i)}(k) : i \in \{1, 2, 3\}, k = 1, \dots, K\}, \quad (9)$$

where $S_{1:T}^{(i)}(k)$ denotes the i -th construction in Eq. (8) for sample k . In the hybrid formulation, all these members are collectively denoted by $R_{1:T}^{\text{ens}}$ and are used for probabilistic evaluation. The ensemble forecasts shown in the result figures correspond to the mean over all ensemble members (see [Supplementary Note 2.3](#) for additional implementation details).

Training and evaluation

Training protocol. The model training proceeds in two stages that mirror the hybrid formulation described above. In the first stage, we train the physics-informed module Θ to produce a deterministic evolution of the radar reflectivity field. In the second stage, we freeze Θ and train the probabilistic refinement module Φ to learn a conditional distribution of futures given both the past observations and the deterministic forecast.

Training the physics-informed module. In the first stage, we optimize all parameters of the physics-informed module Θ , including the shared backbone and the three task-specific decoders. The objective $\mathcal{L}_{\text{phys}}$ is a composite loss that supervises the intermediate states of the operator sequence as well as the final forecast. At each forecast step t , we penalize discrepancies between (i) the purely advected field, (ii) the advected–diffused field and (iii) the final source-corrected forecast and the corresponding ground-truth radar volume at time $t + 1$. The total loss is a weighted sum of ℓ_1 norms accumulated over the forecast horizon, namely,

$$\mathcal{L}_{\text{phys}} = \sum_{t=0}^{T-1} \left(\lambda_{\text{adv}} \mathcal{L}_{\text{adv}}^{(t)} + \lambda_{\text{diff}} \mathcal{L}_{\text{diff}}^{(t)} + \mathcal{L}_{\text{pred}}^{(t)} \right), \quad (10)$$

where

$$\mathcal{L}_{\text{adv}}^{(t)} = \|\mathcal{A}_{\Delta t}[R_t] - R_{t+1}^{\text{truth}}\|_1, \quad (11.1)$$

$$\mathcal{L}_{\text{diff}}^{(t)} = \|\mathcal{D}_{\Delta t}[\mathcal{A}_{\Delta t}[R_t]] - R_{t+1}^{\text{truth}}\|_1, \quad (11.2)$$

$$\mathcal{L}_{\text{pred}}^{(t)} = \|R_{t+1} - R_{t+1}^{\text{truth}}\|_1. \quad (11.3)$$

Here, R_t and R_{t+1} denote the model forecasts at times t and $t + 1$, respectively, and R_{t+1}^{truth} is the corresponding observed radar volume. The weights λ_{adv} and λ_{diff} balance the contribution of the intermediate losses, encouraging the network to learn physically meaningful advection and diffusion operators in addition to accurate end-of-step forecasts. Further training details are provided in [Supplementary Note 3.1](#).

Training the probabilistic refinement module. In the second stage, we train the probabilistic refinement module Φ while keeping Θ fixed. Its dual-branch architecture is designed to produce the structured field S_{struct} and residual field S_{res} used in the ensemble construction in Eq. (8): the structure branch learns a distribution over full future reflectivity fields, whereas the residual branch learns a distribution over corrections to the deterministic forecast.

We train both branches on 2D radar fields rather than on full 3D radar volumes. For each spatiotemporal window, we treat either a single height level or the column-maximum projection as a 2D sample, yielding an augmented training set R^{2D} with corresponding historical, deterministic and truth sequences R_{hist}^{2D} , $R_{1:T}^{2D,\text{det}}$ and $R_{1:T}^{2D,\text{truth}}$.

Each branch is trained as a conditional diffusion model using a shared noise schedule and the v -parameterization [44]. For notational simplicity, we write R_{truth} for $R_{1:T}^{2D,\text{truth}}$ and $r_{\text{truth}} = R_{\text{truth}} - R_{1:T}^{2D,\text{det}}$ for the corresponding residual composites. The 2D conditioning context is given by $c = (R_{-T_0:0}^{2D}, R_{1:T}^{2D,\text{det}})$. Here, τ indexes the diffusion step. We sample $\tau \sim \text{Unif}\{0, \dots, N-1\}$ and $\epsilon \sim \mathcal{N}(0, \mathbf{I})$, where N is the total number of diffusion steps. Let $\{\beta_\tau\}_{\tau=0}^{N-1}$ be the shared noise schedule, $\alpha_\tau = 1 - \beta_\tau$, and $\bar{\alpha}_\tau = \prod_{s=0}^{\tau} \alpha_s$. For each branch, a dedicated context encoder processes c and produces a hierarchy of multi-scale feature maps used to condition the denoiser; we denote these encoded features by $h_{\text{struct}} = E_{\phi_{\text{struct}}}(c)$ and $h_{\text{res}} = E_{\phi_{\text{res}}}(c)$. The structure and residual branches are trained with the following diffusion losses:

$$\mathcal{L}_{\text{struct}} = \mathbb{E}_{\tau, R_{\text{truth}}, \epsilon} \left[\left\| \underbrace{\sqrt{\bar{\alpha}_\tau} \epsilon - \sqrt{1 - \bar{\alpha}_\tau} R_{\text{truth}}}_{v_\tau^{\text{struct}}} - v_{\theta_{\text{struct}}} \left(\underbrace{\sqrt{\bar{\alpha}_\tau} R_{\text{truth}} + \sqrt{1 - \bar{\alpha}_\tau} \epsilon}_{x_\tau^{\text{struct}}}, \tau, h_{\text{struct}} \right) \right\|_2^2 \right], \quad (12.1)$$

$$\mathcal{L}_{\text{res}} = \mathbb{E}_{\tau, r_{\text{truth}}, \epsilon} \left[\left\| \underbrace{\sqrt{\bar{\alpha}_\tau} \epsilon - \sqrt{1 - \bar{\alpha}_\tau} r_{\text{truth}}}_{v_\tau^{\text{res}}} - v_{\theta_{\text{res}}} \left(\underbrace{\sqrt{\bar{\alpha}_\tau} r_{\text{truth}} + \sqrt{1 - \bar{\alpha}_\tau} \epsilon}_{x_\tau^{\text{res}}}, \tau, h_{\text{res}} \right) \right\|_2^2 \right], \quad (12.2)$$

where $\epsilon \sim \mathcal{N}(0, \mathbf{I})$ emphasizes the Gaussian noise, $\bar{\alpha}_\tau$ is the cumulative product of the noise schedule, and $v_{\theta_{\text{struct}}}$ and $v_{\theta_{\text{res}}}$ denote the predicted v -parameters for the structure and residual branches, respectively. Further training details are provided in [Supplementary Note 3.2](#).

Forecast configurations. We evaluate the model performance at two spatial resolutions: 0.04° (coarse) and 0.01° (fine). At both resolutions, we use 256×256 -pixel input patches. For the 0.04° experiments, this corresponds to a $10.24^\circ \times 10.24^\circ$ domain that is representative of province-scale regions. For the 0.01° experiments, it corresponds to a $2.56^\circ \times 2.56^\circ$ domain tailored to high-resolution, city-scale hazards.

Verification metrics. We assess the forecast quality using three complementary metrics. (i) Event detection and localization are quantified using neighborhood CSI at reflectivity thresholds of 20, 30, 40 and 50 dBZ. This metric rewards forecasts that place high-intensity cells close to their observed locations while allowing for small spatial offsets. (ii) Perceptual and structural fidelity are evaluated using the LPIPS metric with a pre-trained AlexNet [45] backbone, which correlates well with human visual judgement of image similarity. (iii) Scale-dependent realism is diagnosed using PSD analysis: we compute the 2D power spectrum of each forecast and observation, perform radial averaging to obtain a 1D spectrum as a function of wavelength, and compare spectral slopes and power ratios from convective to mesoscale ranges.

For a fair comparison with 2D baselines, all three metrics are computed on column-maximum reflectivity fields obtained by applying the same vertical projection to the three-dimensional Nowcast3D forecasts and to the input radar volumes used for the 2D models.

Validation of inferred wind fields. To evaluate the physical realism of the velocity field \mathbf{v} inferred by Nowcast3D (see Eq. (3)), we compare it with independent observations from wind-profiler radars. This requires a two-step post-processing procedure (Extended Data Figure 4a). First, the model output, expressed as grid-cell displacement per 6-min interval in degrees, is converted to zonal and meridional velocity components in ms^{-1} using latitude-dependent scaling to account for spherical geometry. Second, because profiler sites do not coincide exactly with our model grid points, we perform spatiotemporal matching by defining, for each observation, a horizontal search radius and a vertical tolerance window (Extended Data Figure 4b,c). The corresponding model value is obtained by averaging all grid cells within this 3D cylinder at the matching forecast time.

From the resulting matched pairs, we compute the Pearson correlation coefficient between predicted and observed wind speeds over the forecast horizon (Extended Data Figure 4d), as well as the mean absolute error of wind direction (Extended Data Figure 4e). This analysis provides an independent check on the consistency of the inferred flow fields with observed winds in precipitating regions and complements the reflectivity-based verification described above. The velocity field derived from the stream-function and potential-function decomposition is detailed in [Supplementary Note 6.2](#).

Data availability

The three dimensional radar data used in this study to support the training of nowcasting models in China were provided by the China Meteorological Administration (CMA). These data are available from the authors upon reasonable request and with permission from the CMA. A demonstration dataset used in this paper is publicly accessible at <https://github.com/Huaguan-Chen/Nowcast3D>.

Code availability

All the source codes to reproduce the results in this study are available in the GitHub repository at <https://github.com/Huaguan-Chen/Nowcast3D>.

References

- [1] Yuchen Zhang, Mingsheng Long, Kaiyuan Chen, Lanxiang Xing, Ronghua Jin, Michael I Jordan, and Jianmin Wang. Skilful nowcasting of extreme precipitation with NowcastNet. *Nature*, 619(7970):526–532, 2023.
- [2] Mariusz Starzec, Gretchen L Mullendore, and Paul A Kucera. Using radar reflectivity to evaluate the vertical structure of forecast convection. *Journal of Applied Meteorology and Climatology*, 57(12):2835–2849, 2018.
- [3] Gabriele Franch, Valerio Maggio, Luca Coviello, Marta Pendesini, Giuseppe Jurman, and Cesare Furlanello. TAASRAD19, a high-resolution weather radar reflectivity dataset for precipitation nowcasting. *Scientific Data*, 7(1):234, 2020.
- [4] Shigenori Otsuka, Gulanbaier Tuerhong, Ryota Kikuchi, Yoshikazu Kitano, Yusuke Taniguchi, Juan Jose Ruiz, Shinsuke Satoh, Tomoo Ushio, and Takemasa Miyoshi. Precipitation nowcasting with three-dimensional space–time extrapolation of dense and frequent phased-array weather radar observations. *Weather and Forecasting*, 31(1):329–340, 2016.

- [5] Matthias Steiner, Robert A Houze Jr, and Sandra E Yuter. Climatological characterization of three-dimensional storm structure from operational radar and rain gauge data. *34(9):1978–2007*, 1995.
- [6] Michael I Biggerstaff and Steven A Listemaa. An improved scheme for convective/stratiform echo classification using radar reflectivity. *Journal of Applied Meteorology and Climatology*, 39(12):2129–2150, 2000.
- [7] Juanzhen Sun, Ming Xue, James W Wilson, Isztar Zawadzki, Sue P Ballard, Jeanette Onvlee-Hooimeyer, Paul Joe, Dale M Barker, Ping-Wah Li, Brian Golding, et al. Use of NWP for nowcasting convective precipitation: Recent progress and challenges. *Bulletin of the American Meteorological Society*, 95(3):409–426, 2014.
- [8] Kaifeng Bi, Lingxi Xie, Hengheng Zhang, Xin Chen, Xiaotao Gu, and Qi Tian. Accurate medium-range global weather forecasting with 3D neural networks. *Nature*, 619(7970):533–538, 2023.
- [9] Remi Lam, Alvaro Sanchez-Gonzalez, Matthew Willson, Peter Wirnsberger, Meire Fortunato, Ferran Alet, Suman Ravuri, Timo Ewalds, Zach Eaton-Rosen, Weihua Hu, et al. Learning skillful medium-range global weather forecasting. *Science*, 382(6677):1416–1421, 2023.
- [10] Dmitrii Kochkov, Janni Yuval, Ian Langmore, Peter Norgaard, Jamie Smith, Griffin Mooers, Milan Klöwer, James Lottes, Stephan Rasp, Peter Düben, et al. Neural general circulation models for weather and climate. *Nature*, 632(8027):1060–1066, 2024.
- [11] Cristian Bodnar, Wessel P Bruinsma, Ana Lucic, Megan Stanley, Anna Allen, Johannes Brandstetter, Patrick Garvan, Maik Riechert, Jonathan A Weyn, Haiyu Dong, et al. A foundation model for the Earth system. *Nature*, pages 1–8, 2025.
- [12] Xiuyu Sun, Xiaohui Zhong, Xiaoze Xu, Yuanqing Huang, Hao Li, J David Neelin, Deliang Chen, Jie Feng, Wei Han, Libo Wu, et al. A data-to-forecast machine learning system for global weather. *Nature Communications*, 16(1):6658, 2025.
- [13] Yingzhe Cui, Ruohan Wu, Xiang Zhang, Ziqi Zhu, Bo Liu, Jun Shi, Junshi Chen, Hailong Liu, Shenghui Zhou, Liang Su, et al. Forecasting the eddying ocean with a deep neural network. *Nature Communications*, 16(1):2268, 2025.
- [14] Anna Allen, Stratis Markou, Will Tebbutt, James Requeima, Wessel P Bruinsma, Tom R Andersson, Michael Herzog, Nicholas D Lane, Matthew Chantry, J Scott Hosking, et al. End-to-end data-driven weather prediction. *Nature*, 641(8065):1172–1179, 2025.
- [15] Seppo Pulkkinen, Daniele Nerini, Andrés A Pérez Hortal, Carlos Velasco-Forero, Alan Seed, Urs Germann, and Loris Foresti. Pysteps: An open-source Python library for probabilistic precipitation nowcasting (v1. 0). *Geoscientific Model Development*, 12(10):4185–4219, 2019.
- [16] Suman Ravuri, Karel Lenc, Matthew Willson, Dmitry Kangin, Remi Lam, Piotr Mirowski, Megan Fitzsimons, Maria Athanassiadou, Sheleem Kashem, Sam Madge, et al. Skillful precipitation nowcasting using deep generative models of radar. *Nature*, 597(7878):672–677, 2021.
- [17] Zhangyang Gao, Cheng Tan, Lirong Wu, and Stan Z. Li. Simvp: Simpler yet better video prediction. In *Proceedings of the IEEE/CVF Conference on Computer Vision and Pattern Recognition*, pages 3170–3180, June 2022.

- [18] Xingjian Shi, Zhourong Chen, Hao Wang, Dit-Yan Yeung, Wai-Kin Wong, and Wang-chun Woo. Convolutional LSTM network: A machine learning approach for precipitation nowcasting. In *Advances in Neural Information Processing Systems*, volume 28, 2015.
- [19] Yunbo Wang, Mingsheng Long, Jianmin Wang, Zhifeng Gao, and Philip S Yu. PredRNN: Recurrent neural networks for predictive learning using spatiotemporal LSTMs. In *Advances in Neural Information Processing Systems*, pages 879–888, 2017.
- [20] Zhihan Gao, Xingjian Shi, Hao Wang, Yi Zhu, Yuyang Wang, Mu Li, and Dit-Yan Yeung. Earthformer: Exploring space-time transformers for earth system forecasting. In *Advances in Neural Information Processing Systems*, pages 25390–25403, 2022.
- [21] Lasse Espeholt, Shreya Agrawal, Casper Sønderby, Manoj Kumar, Jonathan Heek, Carla Bromberg, Cenk Gizen, Rob Carver, Marcin Andrychowicz, Jason Hickey, et al. Deep learning for twelve hour precipitation forecasts. *Nature Communications*, 13(1):5145, 2022.
- [22] Puja Das, August Posch, Nathan Barber, Michael Hicks, Kate Duffy, Thomas Vandal, Debjani Singh, Katie van Werkhoven, and Auroop R Ganguly. Hybrid physics-AI outperforms numerical weather prediction for extreme precipitation nowcasting. *npj Climate and Atmospheric Science*, 7(1):282, 2024.
- [23] Fabio Sgrist, Hans R Künsch, and Werner A Stahel. Stochastic partial differential equation based modelling of large space–time data sets. *Journal of the Royal Statistical Society Series B: Statistical Methodology*, 77(1):3–33, 2015.
- [24] H. Helmholtz. Über integrale der hydrodynamischen gleichungen, welche den wirbelbewegungen entsprechen. *Journal für die reine und angewandte Mathematik*, 55:25–55, 1858.
- [25] Jie Cao, Lingkun Ran, and Na Li. An application of the Helmholtz theorem in extracting the externally induced deformation field from the total wind field in a limited domain. *Monthly Weather Review*, 142(5):2060–2066, 2014.
- [26] Lanxiang Xing, Haixu Wu, Yuezhou Ma, Jianmin Wang, and Mingsheng Long. Helmfluid: Learning helmholtz dynamics for interpretable fluid prediction. In *International Conference on Machine Learning*, 2024.
- [27] Jonathan Ho, Ajay Jain, and Pieter Abbeel. Denoising diffusion probabilistic models. In *Advances in Neural Information Processing Systems*, volume 33, pages 6840–6851, 2020.
- [28] Jiaming Song, Chenlin Meng, and Stefano Ermon. Denoising Diffusion Implicit Models. In *9th International Conference on Learning Representations*, 2021.
- [29] Junchao Gong, Lei Bai, Peng Ye, Wanghan Xu, Na Liu, Jianhua Dai, Xiaokang Yang, and Wanli Ouyang. Cascast: Skillful high-resolution precipitation nowcasting via cascaded modelling. In *International Conference on Machine Learning*, pages 15809–15822. PMLR, 2024.
- [30] Demin Yu, Xutao Li, Yunming Ye, Baoquan Zhang, Chuyao Luo, Kuai Dai, Rui Wang, and Xunlai Chen. Diffcast: A unified framework via residual diffusion for precipitation nowcasting. In *Proceedings of the IEEE/CVF Conference on Computer Vision and Pattern Recognition*, pages 27758–27767, 2024.

- [31] Ilan Price, Alvaro Sanchez-Gonzalez, Ferran Alet, Tom R Andersson, Andrew El-Kadi, Dominic Masters, Timo Ewalds, Jacklynn Stott, Shakir Mohamed, Peter Battaglia, et al. Probabilistic weather forecasting with machine learning. *Nature*, 637(8044):84–90, 2025.
- [32] Lizao Li, Robert Carver, Ignacio Lopez-Gomez, Fei Sha, and John Anderson. Generative emulation of weather forecast ensembles with diffusion models. *Science Advances*, 10(13):eadk4489, 2024.
- [33] Ian T Jolliffe and David B Stephenson. *Forecast verification: a practitioner’s guide in atmospheric science*. John Wiley & Sons, 2011.
- [34] S Sinclair and GGS Pegram. Empirical Mode Decomposition in 2-D space and time: a tool for space-time rainfall analysis and nowcasting. *Hydrology and Earth System Sciences*, 9(3):127–137, 2005.
- [35] Richard Zhang, Phillip Isola, Alexei A Efros, Eli Shechtman, and Oliver Wang. The unreasonable effectiveness of deep features as a perceptual metric. In *Proceedings of the IEEE/CVF Conference on Computer Vision and Pattern Recognition*, pages 586–595, 2018.
- [36] James E Matheson and Robert L Winkler. Scoring rules for continuous probability distributions. *Management Science*, 22(10):1087–1096, 1976.
- [37] Hans Hersbach. Decomposition of the continuous ranked probability score for ensemble prediction systems. *Weather and Forecasting*, 15(5):559–570, 2000.
- [38] Olaf Ronneberger, Philipp Fischer, and Thomas Brox. U-Net: Convolutional Networks for Biomedical Image Segmentation. In *International Conference on Medical Image Computing and Computer Assisted Intervention*, pages 234–241. Springer, 2015.
- [39] Ashish Vaswani, Noam Shazeer, Niki Parmar, Jakob Uszkoreit, Llion Jones, Aidan N Gomez, Łukasz Kaiser, and Illia Polosukhin. Attention Is All You Need. *Advances in Neural Information Processing Systems*, 30, 2017.
- [40] Andrew Staniforth and Jean Côté. Semi-Lagrangian integration schemes for atmospheric models—A review. *Monthly Weather Review*, 119(9):2206–2223, 1991.
- [41] Albert Einstein. Über die von der molekularkinetischen Theorie der Wärme geforderte Bewegung von in ruhenden Flüssigkeiten suspendierten Teilchen. *Annalen der Physik*, 4, 1905.
- [42] Sydney Chapman and Thomas George Cowling. *The Mathematical Theory of Non-Uniform Gases: an account of the kinetic theory of viscosity, thermal conduction and diffusion in gases*. Cambridge University Press, 1990.
- [43] Rui Zhang, Qi Meng, Rongchan Zhu, Yue Wang, Wenlei Shi, Shihua Zhang, Zhi-Ming Ma, and Tie-Yan Liu. Monte carlo neural PDE solver for learning PDEs via probabilistic representation. *IEEE Transactions on Pattern Analysis and Machine Intelligence*, 2025.
- [44] Tim Salimans and Jonathan Ho. Progressive distillation for fast sampling of diffusion models. In *International Conference on Learning Representations*, 2022.
- [45] Alex Krizhevsky, Ilya Sutskever, and Geoffrey E Hinton. Imagenet classification with deep convolutional neural networks. *Advances in Neural Information Processing Systems*, 25, 2012.

Acknowledgement

The work is supported by the National Natural Science Foundation of China (62276269, 92270118), the Beijing Natural Science Foundation (1232009), the National Key Research and Development Program of China (2025YFE0217100), and the Strategic Priority Research Program of the Chinese Academy of Sciences (XDB0620103). We sincerely thank Professor Xiaoding Yu, for his important contribution to the meteorologist evaluation process. We also extend our heartfelt thanks to the 160 anonymous meteorologists who participated in the meteorologist evaluation.

Author contributions

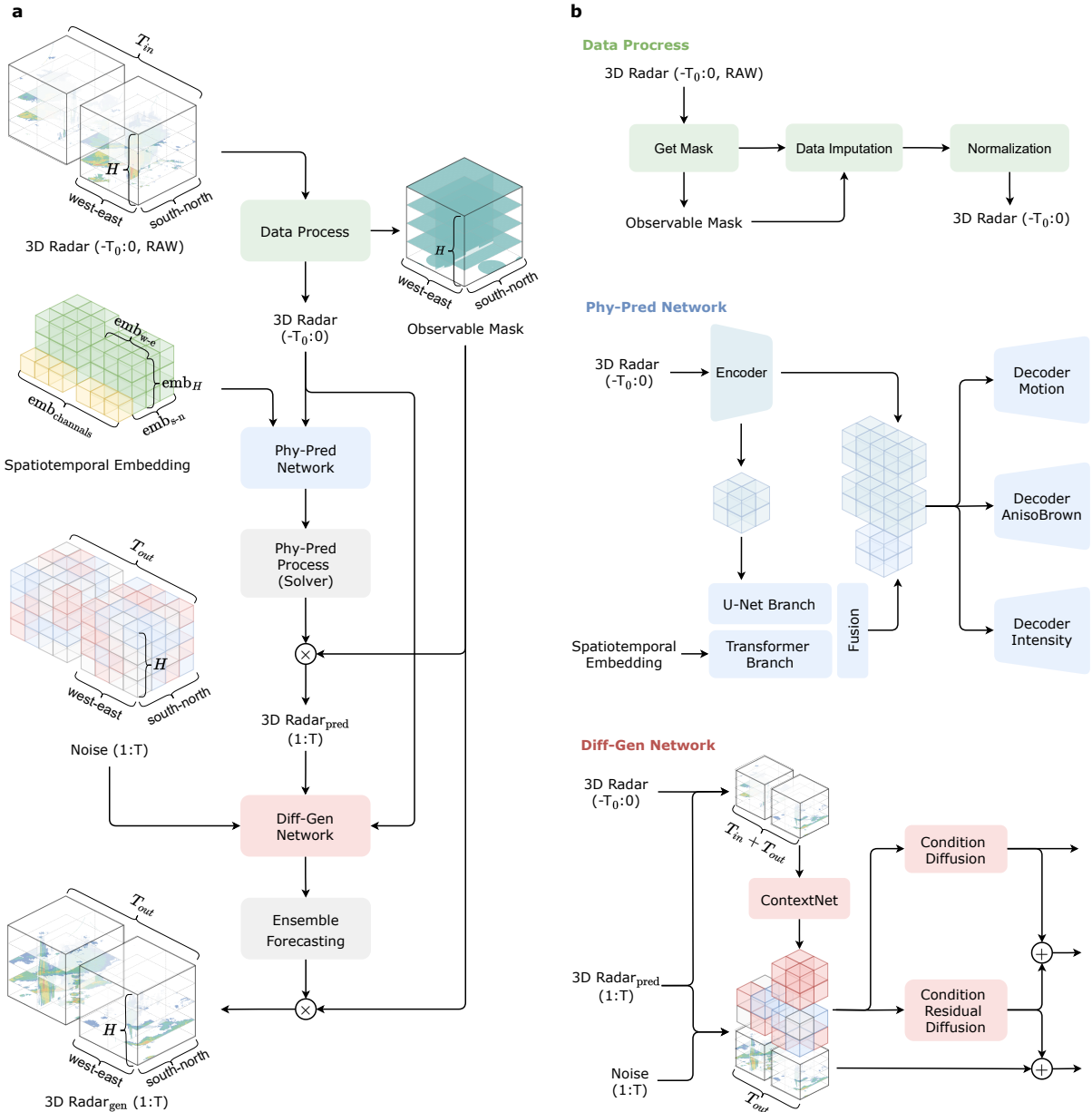
H.S. (Hao Sun) and W.H. organized and led the project. H.S. (Hao Sun), W.H., and H.C. explored and designed the model and methodology. H.C. developed the Nowcast3D framework, including model architecture, training, and fine-tuning. H.S. (Haofei Sun), Y.Y., and H.C. collected and processed the radar data, while X.S. provided the wind profiler radar data. J.T. and H.C. conducted case studies and analyzed the results. N.L. contributed to the preliminary development and conceptualization of the study. H.S. (Hao Sun) and W.H. supervised all aspects of the project. All authors participated in the writing and revision of the manuscript.

Corresponding authors

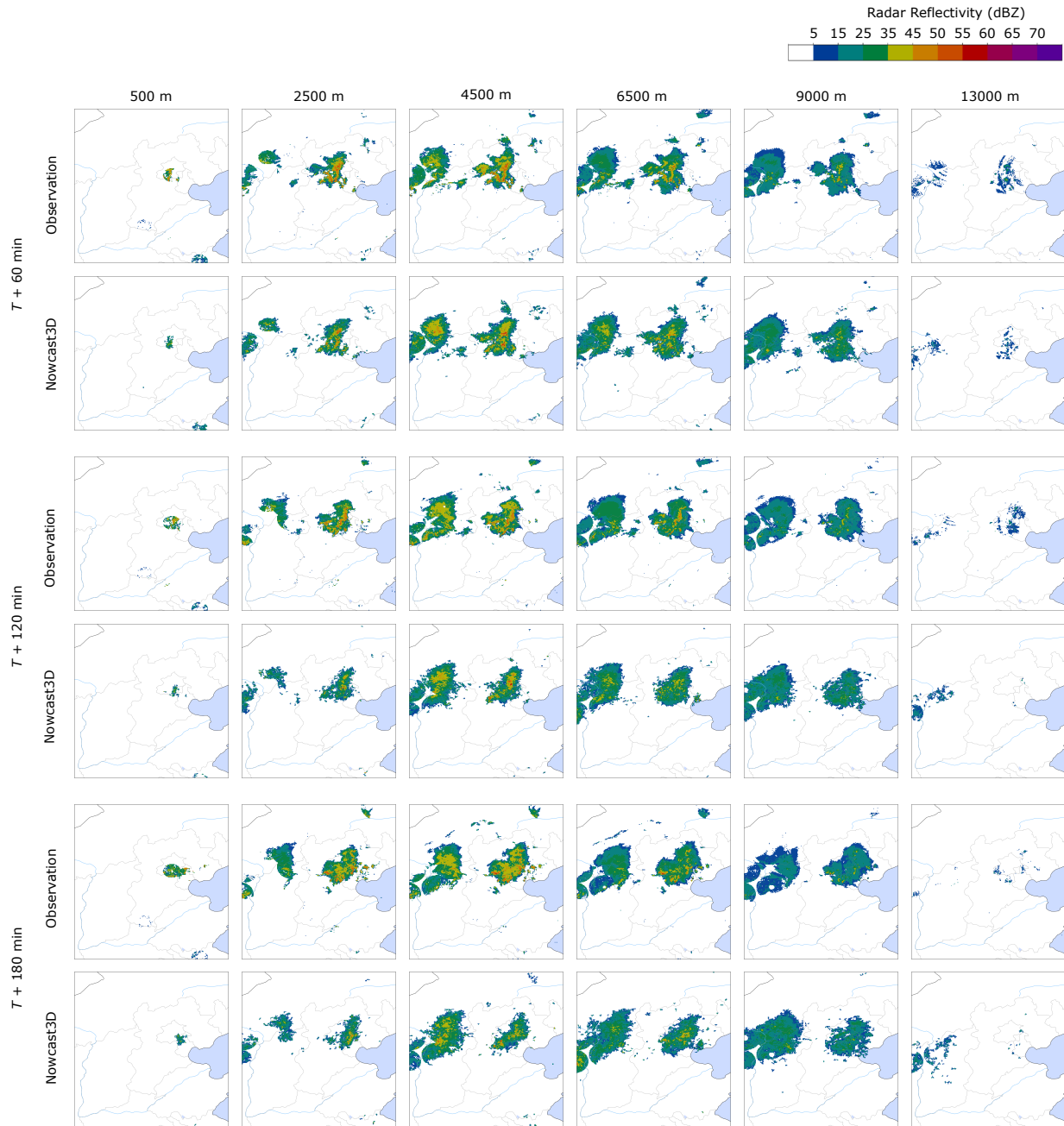
Hao Sun (haosun@ruc.edu.cn) and Wei Han (hanwei@cma.gov.cn).

Competing interests

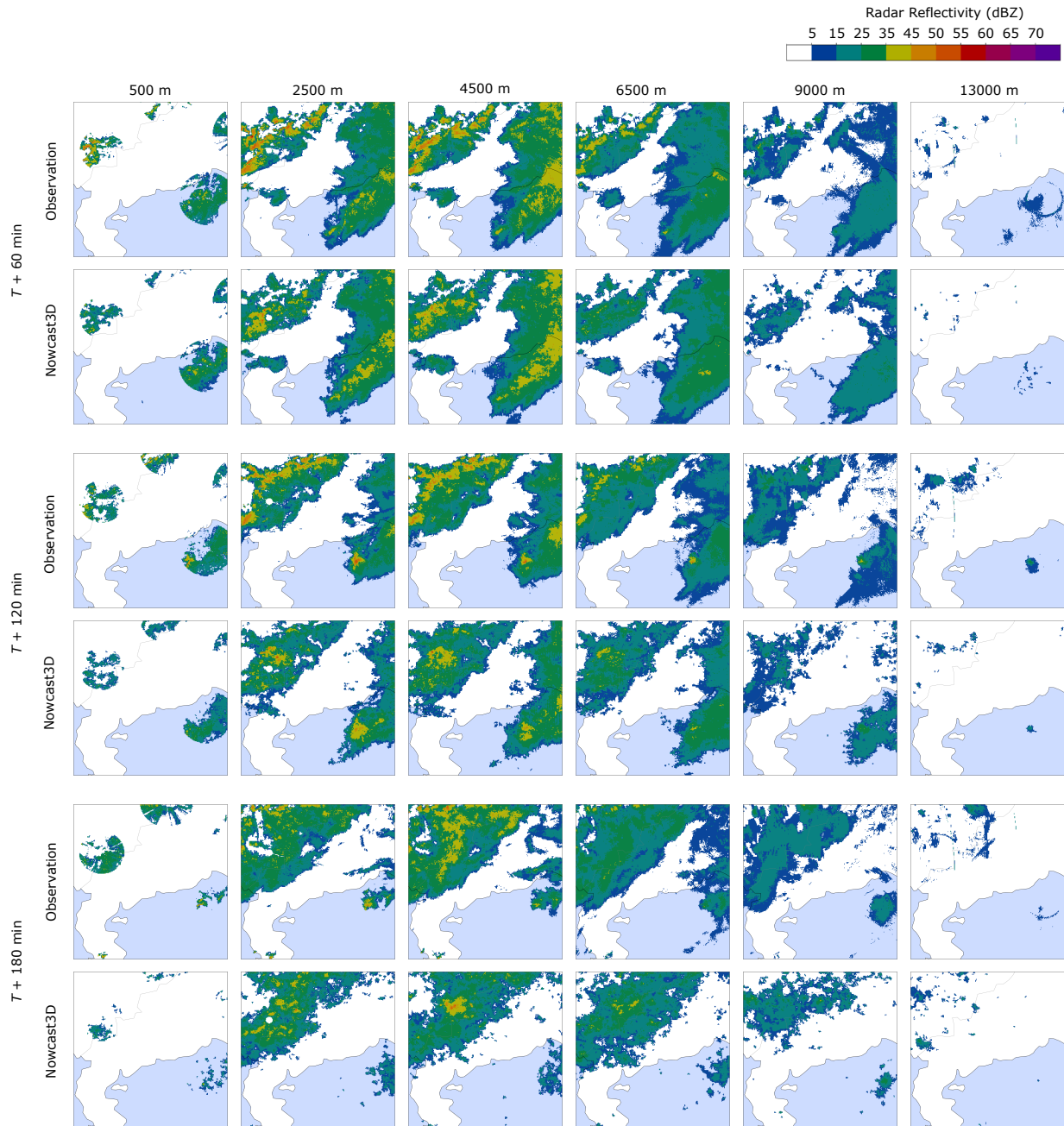
The authors declare no competing interests.



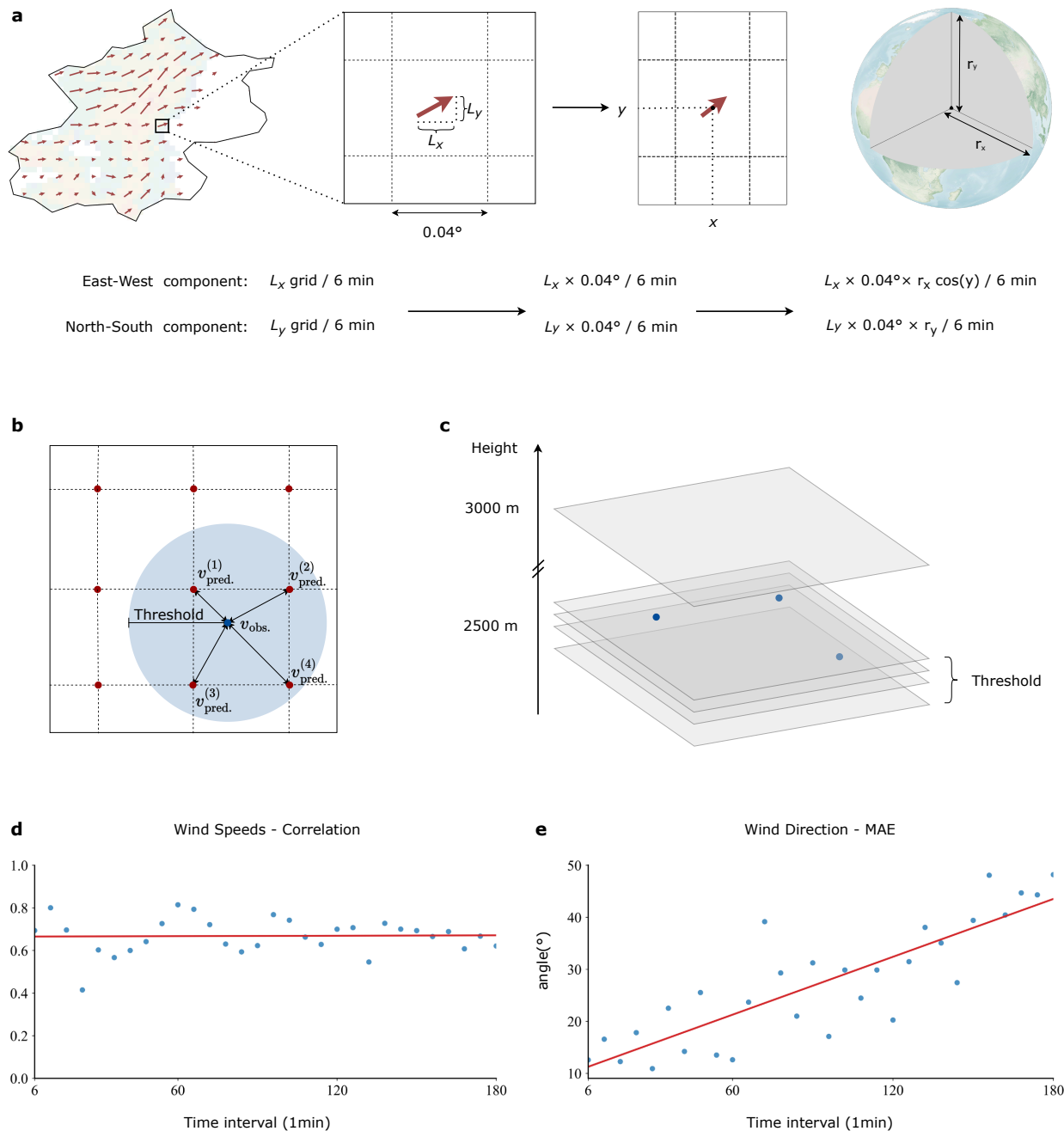
Extended Data Figure 1: Overview of the Nowcast3D framework. The pipeline consists of three main components: data processing (green), a physics-based prediction network (blue) and a diffusion-based generative refinement network (red). **a**, Pipeline of Nowcast3D. Raw 3D radar volumes spanning the period of $T_{in} = [-T_0 : 0]$ are processed into normalized inputs and an observable mask, while spatiotemporal embeddings are provided as external inputs. Phy-Pred produces a coarse forecast Radar^{pred} ($1:T$), which is refined by Diff-Gen with injected noise to generate Radar^{gen}, followed by ensemble aggregation. **b**, Module details. Data processing performs mask extraction, masked imputation, and normalization. Phy-Pred fuses U-Net and Transformer branches with decoders for motion, anisotropic Brownian components, and intensity. Diff-Gen uses ContextNet and conditional diffusion on the structure and residual, conditioned on the input and Radar^{pred}.



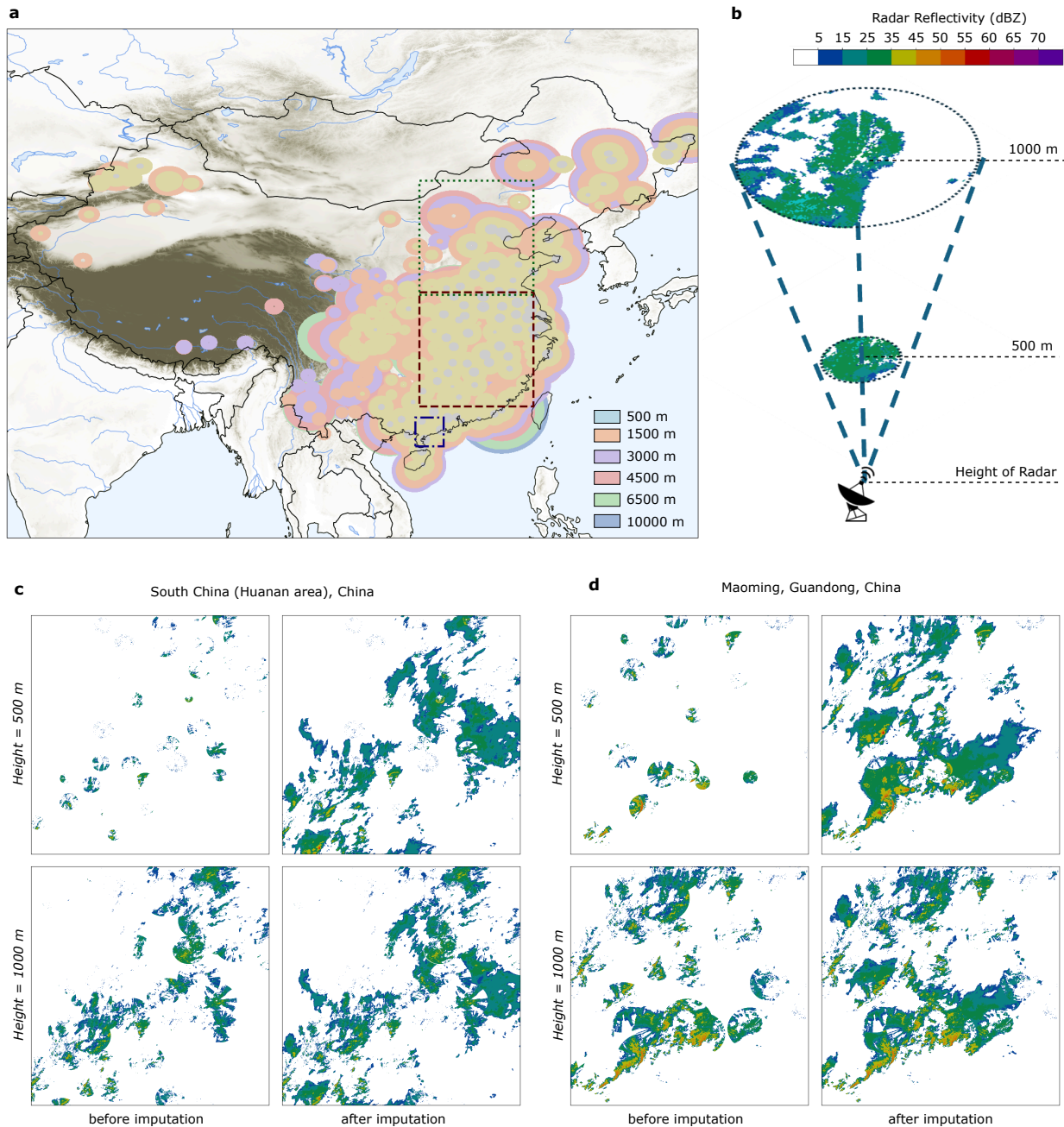
Extended Data Figure 2: Nowcast3D’s layered forecasts of an extreme precipitation event in North China at 60, 120, and 180 min lead times, for altitudes ranging from 500 m to 13,000 m. This figure shows the layered prediction maps corresponding to Figure 2. We show a comparison between our prediction results and the ground truth (radar observations) at a specific vertical height. The observation at 500 m exhibits circular features due to the limitation of radar detection range, which appears as an overlap of multiple observation circles at low altitudes.



Extended Data Figure 3: Nowcast3D’s layered forecasts of an extreme precipitation event in Maoming, Guangdong Province, China at 60, 120, and 180 min lead times, for altitudes ranging from 500 m to 13,000 m. This figure shows the layered prediction maps corresponding to in Figure 3. We show a comparison between our prediction results and the ground truth (radar observations) at a specific vertical height. The observation at 500 m exhibits circular features due to the limitations of the radar detection range, which appears as an overlap of multiple observation circles at low altitudes.



Extended Data Figure 4: Wind field estimation of Nowcast3D forecast. **a**, Schematic of calculation from gridded data to site-specific wind field. **b**, Spatial averaging for evaluation: because observation sites do not exactly align with grid points, we define a circular area with a radius of **Threshold** around each site. The predicted values inside this circle are averaged for comparison with the site's observation. **c**, Vertical averaging for evaluation: as observations may not match the exact vertical levels of the predictions, we average all observations within a vertical range of $\pm \text{Threshold} / 2$ at a specific height for comparison. **d**, Temporal evolution of the correlation coefficient between predicted and observed wind speeds. **e**, Temporal evolution of the mean absolute error in wind direction between predicted and observed winds.



Extended Data Figure 5: Radar network coverage and low-level imputation examples. **a**, Spatial distribution of the operational weather radar network over China and surrounding regions, with colored disks indicating approximate horizontal coverage at 500, 1500, 3000, 4500, 6500 and 10,000 m above the sea level. The dashed rectangle marks the analysis domain used in this study. **b**, Schematic of 3D radar sampling, illustrating how the beam widens with range and leads to sparse coverage near the surface despite dense sampling aloft. **c**, Example of low-level reflectivity in South China (the Huanan area) at attitudes of 500 m and 1,000 m before (left) and after (right) imputation. **d**, Same as **c** but for a convective event near Maoming, Guangdong Province, China, highlighting the recovery of coherent low-level structures beneath well-observed upper-level echoes.